A localized-basis scheme for molecular dynamics

1993 J. Phys.: Condens. Matter 5 1055

(http://iopscience.iop.org/0953-8984/5/8/008)

J. Phys.: Condens. Matter 4 (1992) 1055–1080. Printed in the UK

A localized-basis scheme for molecular dynamics

Zijing Lin and J Harris

Institut für Festkörperforschung, Forschungszentrum Jülich GmbH, D-5170 Jülich, Federal Republic of Germany

Received 7 October 1992

Abstract. The combination of molecular dynamics and density-functional theory introduced by Car and Parrinello (CP) has broadened very markedly the range of systems and properties that can be treated on a first-principles basis. The CP formulation involves plane-wave expansions for wavefunctions and potentials and is best suited when the atoms can be represented by weak pseudopotentials. An alternative approach employs expansions in localized orbitals and may prove advantageous where strong potentials are encountered. The approach derives forces from a density functional closely related to the Kohn–Sham functional but defined rigorously on function space, in particular for a sum of site densities. This simplifies force calculation substantially. The site densities are represented via a density basis and the orbitals by an orbital basis of exponentially localized A-functions whose exponents are optimized dynamically. The potential of the approach is demonstrated via explicit calculations, including molecular-dynamics simulations for hydrogen clusters.

1. Introduction

The molecular-dynamics–density-functional method (MD–DF) of Car and Parrinello (1985) (CP) involves two essential elements. (i) The potential, $E[\boldsymbol{R}_i]$, that governs the nuclear motion is taken to be the density functional of Kohn and Sham (1965), $E_{\mathrm{KS}}[n(\boldsymbol{x}), \boldsymbol{R}_i]$. Here, $\boldsymbol{R}_i$ are the nuclear locations and $n(\boldsymbol{x})$ the electron density. This functional obeys an absolute minimum principle and its minimum value for a given set of $\boldsymbol{R}_i$ is a best estimate of the electronic ground-state energy for these $\boldsymbol{R}_i$ and so represents a point on the adiabatic energy surface for the nuclear motion. (ii) The minimum property is maintained during an MD simulation via *dynamical* propagation of electronic degrees of freedom on a timescale that is fast compared with the nuclear motion. Heavy-mass nuclear degrees of freedom and light-mass electronic degrees of freedom are propagated together according to the laws of classical mechanics in such a way as to maintain the energy functional close to its minimum value. The forces acting on the nuclei then correspond to the adiabatic energy surface. The resulting calculational scheme combines the full power of molecular-dynamics methods, developed over many years for systems that are characterized by simple interactions such as pairwise sums, with a first-principles (though approximate) determination of the relevant forces in systems with chemical interactions.

Because of its simplicity, accuracy and ease of implementation, the plane-wave method is clearly the method of choice for atoms representable by weak pseudopotentials. For most atoms of the periodic table this requires a separation

0953-8984/92/081055+26$07.50

of the wavefunctions into 'stiff' and 'soft' parts, with only the latter described by plane waves in conjunction with 'soft pseudopotentials' (Vanderbilt 1990). Where strong potentials are encountered, expansions in site-localized functions rather than plane waves would seem more appropriate. Such expansions are universal in quantum chemistry and quantum-chemistry-based density-functional work on molecules, and a variety of localized or partially localized functions of varying degrees of sophistication (e.g. muffin-tin orbitals, augmented plane waves) have been used in solid-state and film calculations. These methods are, however, tailored to accurate pointwise energy evaluation rather than the fast calculation of forces. Since site-localized orbitals move with the nuclei, the basis changes as the nuclear positions change resulting in 'Pulay forces' whose computation can be exceedingly time consuming. An orbital basis designed for accurate energy evaluation may therefore be poorly adapted to force computation. Any successful localized basis MD scheme must place the focus the other way around with the main emphasis on fast force calculation, if necessary at the expense of accurate energy evaluation. Some localized-basis schemes have been proposed that are adapted to the specific requirements of MD (Seifert *et al* 1986, Pederson *et al* 1988, Sankey and Niklewski 1989). These schemes appear to give good results in practice, but involve approximations whose consequences are not easy to assess and that restrict possibilities for systematic improvement. In the present paper, we describe a localized-basis MD scheme that also involves approximations but is considerably less restrictive with regard to accuracy and flexibility. Some elements of the scheme as it applies to systems having a single electronic level have been outlined previously (Harris and Hohl 1990). The present paper deals with the many-level problem and extends the scheme so that it applies, potentially, to an arbitrary collection of atoms. The method is based on a density functional that is closely related to the Kohn–Sham functional, but is defined on function space with no 'V-representability' requirement (Harris 1985). This is discussed in section 2 along with some other basic elements of the method. The orbital basis we advocate as optimizing accuracy and ease of calculation—the Λ-functions (Filter and Steinborn 1980, Trivedi and Steinborn 1982)—is described in section 3, where we discuss the evaluation of matrix elements needed for the forces and the energy. Mathematical details, including modifications to treat frozen cores, are treated collectively in the appendices. The relative accuracy of the scheme is discussed in section 4 in connection with explicit calculations for first-row homonuclear dimers. The practicality of the MD scheme is then demonstrated in section 5, where we give results of simulations carried out with collections of 16 and 128 H atoms confined in a box.

2. Basic elements

The CP scheme draws adiabatic forces from the Kohn–Sham functional

$$E_{\mathrm{KS}}[n_{\mathrm{out}}] = \sum_n a_n \epsilon_n + E_{\mathrm{N}} + \int \mathrm{d}\boldsymbol{x}\; n_{\mathrm{out}}(\boldsymbol{x}) \times \left\{ \tfrac{1}{2}\phi_{\mathrm{out}}(\boldsymbol{x}) + \epsilon_{\mathrm{xc}}[n_{\mathrm{out}}(\boldsymbol{x})] + V_{\mathrm{ext}}(\boldsymbol{x}) - V_{\mathrm{eff}}(\boldsymbol{x}) \right\} \tag{1}$$

where the a_n are occupation numbers, $\phi_{\mathrm{out}}(\boldsymbol{x})$ is the Coulomb potential associated with density $n_{\mathrm{out}}(\boldsymbol{x})$, $\epsilon_{\mathrm{xc}}[n]$ is the local-density approximation (LDA) exchange–correlation energy density, V_{ext} is the nuclear potential, E_{N} the internuclear repulsion,

and ϵ_n are the eigenvalues of the one-particle Schrödinger equation with potential $V_{\rm eff}(\boldsymbol{x})$. The density $n_{\rm out}(\boldsymbol{x})$ is constructed from the occupied orbitals of this equation as usual. In the CP plane-wave method these orbitals are expanded in plane waves and the coefficients are treated as classical dynamical variables having a small mass. Propagation of these variables along with the nuclear coordinates and under appropriate conditions allows maintenance of adiabaticity where the functional in equation (1) is kept at or close to its local minimum. The crucial advantage of plane waves is the availability of fast-Fourier-transform routines whose time requirement grows essentially linearly with vector length.

The alternative approach we propose takes as its starting point a density functional, $E[n]$, that is closely related to the Kohn–Sham functional but has some advantages if the basis used to solve the one-particle Schrödinger equation consists of localized orbitals (Harris 1985, Foulkes and Haydock 1989). $E[n]$ is stationary at the same density as $E_{\rm KS}[n]$ but, unlike this functional, can be assigned a value for an arbitrary density, in particular a density constructed by summing spherically symmetric site densities centred on the atoms. Specifically,

$$E[n] = \sum_n a_n \tilde{\epsilon}_n - \int {\rm d}\boldsymbol{x}\; n(\boldsymbol{x})\left\{\tfrac{1}{2}\phi(\boldsymbol{x}) + \mu_{\rm xc}[n(\boldsymbol{x})] - \epsilon_{\rm xc}[n(\boldsymbol{x})]\right\} + E_{\rm N} \tag{2}$$

where $\mu_{\rm xc}(n) \equiv {\rm d}(n\epsilon_{\rm xc})/{\rm d}n$ is the exchange–correlation potential and the eigenvalues $\tilde{\epsilon}_n$ are those resulting when the one-particle Schrödinger equation is solved with potential

$$V_n(\boldsymbol{x}) = \phi(\boldsymbol{x}) + \mu_{\rm xc}[n(\boldsymbol{x})] + V_{\rm ext}(\boldsymbol{x}). \tag{3}$$

To evaluate $E[n]$ for given $n(\boldsymbol{x})$ and $\boldsymbol{R}_i$ it is necessary only to calculate the eigenvalues for a specific one-particle potential. The eigenvectors do not appear explicitly in the energy expression and, in particular, the Coulomb potential corresponding to these eigenvectors need not be calculated. This is an important advantage when the orbital basis is localized because the calculation of the electrostatic energy corresponding to the 'out density' then requires four-centre integrals. This problem is eliminated entirely on using $E[n]$ in connection with an appropriately tailored density representation such as a sum over spherically symmetric site densities, for which the evaluation of the electrostatic energy is straightforward. A number of calculations have illustrated that the quadratic error made in using $E[n]$ in conjunction with a sum over site densities can be small, and that the value of $E[n]$ about its stationary point depends only weakly on deviations of n from its optimum value (Polatoglou and Methfessel 1988, 1990, Read and Needs 1989, Finnis 1990).

A further property of $E[n]$ that is vital to its usefulness in MD was conjectured by Finnis (1990) on the basis of calculational experience. This is that for a wide class of density variations, in particular including sums over spherically symmetric site densities, $E[n]$ displays a maximum at its stationary point. The stationarity properties of $E[n]$ were studied in detail by Zaremba (1990) and considered further by Robertson and Farid (1991). This work established that, within the LDA, $E[n]$ displays a saddle point at its extremum and has positive and negative curvature for density fluctuations consisting primarily of long- and short-wavelength components. The cross-over in sign of the curvature is due to the LDA exchange–correlation energy outweighing the electrostatic energy at short wavelengths. It is of course vital for MD

applications that the sign of the curvature of E about its stationary point remain constant. This can be negative or positive but must not switch from one to the other during a simulation. Fortunately, the region of density space over which a positive curvature (dominance of the electrostatic energy) can be guaranteed is large and restrictions that ensure that trial densities remain within this region are minor. That $E[n]$ has a saddle point rather than an absolute maximum therefore implies only some limitations on the degree to which trial densities can be fine tuned.

Variation of the density to ensure $E[n]$ is close to its stationary point can be carried out dynamically in the CP spirit via the following procedure. Restrict the trial density to a sum over sites of the form

$$n(x) = \sum_i n_{\lambda_i}(|x - R_i|) \tag{4}$$

where $n_{\lambda_i}(x)$ is a spherically symmetric site density depending on a parameter λ_i. This is the simplest possible case, and it is quite straightforward to generalize the representation, e.g. several parameters per site, weighting factors that take account of charge transfer, non-spherical terms or 'empty site' densities that describe intra-atomic polarization. The variational freedom of the density representation is restricted only by the requirement that the electrostatic cost of any variation exceed the exchange–correlation gain. Since the functional $E[n]$ is extremely flat about its stationary point a simple representation like equation (4) is less limiting than may be supposed (see section 4). For simplicity of notation we will denote all parameters pertaining to site density i by the single symbol λ_i. Within this restricted space, the functional $E[n]$ goes over to a function, $E(\lambda_i, R_i)$, of discrete variables comprising the trial density parameters and the nuclear coordinates. Adiabatic MD calculations can then be carried out on treating the λ_i as dynamical variables having a negative mass $-M_{\lambda_i}$ so that they will be driven continuously towards the maximum of E. If a simulation is started with optimal (or 'adiabatic') λ_i values, corresponding to the maximum of $E(\lambda_i, R_i^0)$ for the initial nuclear coordinates, R_i^0, and if the natural frequency of the λ motion is larger than that of the nuclear motion (achieved via tuning of the mass ratio), the λ_i^t will oscillate on a short timescale about their local adiabatic values so that the forces acting on the nuclei are always very close to the values they would have if $E[n]$ were maximized in every time step. (The principle is precisely that which pins the moon to the earth as both perform the same orbit around the sun.) Dynamical maintenance of adiabaticity amounts, in density-functional language, to automatic maintenance of 'self-consistency'.

The evaluation of energy and force requires the determination in each time step of the occupied eigenvalues and eigenvectors of a one-particle Schrödinger equation. As mentioned, sophisticated methods have been developed over the past decade to treat this problem, but are poorly adapted to force calculation. Accordingly, we take a step backwards and invoke a representation of the eigenvectors of the LCAO (linear combination of atomic orbitals) form, involving site-localized orbitals $|i\rangle$ depending on exponent parameters α_i. We postpone a detailed consideration of the form these functions should take and note here how the remaining parts of the localized-basis MD scheme are addressed. Within the basis defined by $|i\rangle$, the eigenvectors of the Schrödinger equation are represented by the coefficients C_i^n that solve the matrix eigenvalue problem

$$\{H_{ij} - \epsilon_n \Theta_{ij}\} C_j^n = 0 \qquad H_{ij} = \langle i|\hat{T} + V_n|j\rangle \qquad \Theta_{ij} = \langle i|j\rangle \tag{5}$$

where $\hat{T}$ is the kinetic energy of the electrons, V_n the potential in equation (3) evaluated with the sum over sites density, equation (4), and where a sum over repeated indices is assumed (as in all following equations). In the same representation, the energy functional $E[n]$ takes the form

$$E(\lambda_i, \alpha_i, \boldsymbol{R}_i) = \sum_n \tilde{a}_n C_i^n H_{ij} C_j^n - \int \mathrm{d}\boldsymbol{x}\ n(\boldsymbol{x}) \times \left\{ \tfrac{1}{2}\phi(\boldsymbol{x}) + \mu_{\mathrm{xc}}[n(\boldsymbol{x})] - \epsilon_{\mathrm{xc}}[n(\boldsymbol{x})] \right\} + E_{\mathrm{N}} \tag{6}$$

where $\tilde{a}_n \equiv a_n / [C_i^n \Theta_{ij} C_j^n]$ and $n(\boldsymbol{x})$ is the density in equation (4). The energy now depends on a further set of discrete variables, the exponents, α_i, of the orbitals $|i\rangle$. Since the only term in the energy which depends on these parameters is the ground-state energy of non-interacting electrons in a fixed potential, $E(\lambda_i, \alpha_i, \boldsymbol{R}_i)$ obeys a global minimum with respect to variation of the α_i. In $\{\lambda_i, \alpha_i\}$ space, therefore, E displays a saddle point characterized by positive and negative curvature with respect to λ_i and α_i, respectively. If the exponents are now regarded as dynamical variables and given a positive mass, M_{α_i}, their propagation together with negative-mass λ_i degrees of freedom will result in the continuous maintenance of E at its local saddle point. This amounts to automatic 'self-consistency' *and* 'orbital exponent optimization'.

Adiabatic dynamics can then be achieved by using the Lagrangian

$$\mathcal{L}[\boldsymbol{R}_i, \dot{\boldsymbol{R}}_i, \lambda_i, \dot{\lambda}_i, \alpha_i, \dot{\alpha}_i] = \tfrac{1}{2} \sum_i \left[M_i \dot{\boldsymbol{R}}_i^2 - M_{\lambda_i} \dot{\lambda}_i^2 + M_{\alpha_i} \dot{\alpha}_i^2 \right] - E(\lambda_i, \alpha_i, \boldsymbol{R}_i) \tag{7}$$

along with an appropriate choice for the auxiliary masses that ensure the λ and α motion is faster than the motion of the nuclear coordinates. The equations of motion,

$$M_i \ddot{\boldsymbol{R}}_i = -\nabla_{\boldsymbol{R}_i} E \qquad M_{\lambda_i} \ddot{\lambda}_i = \frac{\partial E}{\partial \lambda_i} \qquad M_{\alpha_i} \ddot{\alpha}_i = -\frac{\partial E}{\partial \alpha_i} \tag{8}$$

involve forces that are readily determined by direct differentiation of $E(\lambda_i, \alpha_i, \boldsymbol{R}_i)$. The λ and α forces are given by

$$\begin{aligned} \frac{\partial E}{\partial \lambda_k} &= \sum_n \tilde{a}_n C_i^n \frac{\partial V_{ij}}{\partial \lambda_k} C_j^n - \int \mathrm{d}\boldsymbol{x}\ n(\boldsymbol{x}) \frac{\partial V_n(\boldsymbol{x})}{\partial \lambda_k} \\ \frac{\partial E}{\partial \alpha_k} &= \sum_n \tilde{a}_n C_i^n \left(\frac{\partial H_{ij}}{\partial \alpha_k} - \epsilon_n \frac{\partial \Theta_{ij}}{\partial \alpha_k} \right) C_j^n \end{aligned} \tag{9}$$

where the derivatives of H_{ij} and Θ_{ij} are zero unless $k = i, j$ because the potential in the one-particle Schrödinger equation is independent of the α_i. The forces on the nuclei comprise three terms,

$$\begin{aligned} \nabla_{\boldsymbol{R}_k} E(\lambda_i, \alpha_i, \boldsymbol{R}_i) &= Z_k \nabla_{\boldsymbol{R}_k} \sum_i \Phi_{\lambda_i}(|\boldsymbol{R}_k - \boldsymbol{R}_i|) + \sum_n \tilde{a}_n C_i^n \langle i | \nabla_{\boldsymbol{R}_k} V_n | j \rangle C_j^n \\ &\quad - \int \mathrm{d}\boldsymbol{x}\ n(\boldsymbol{x}) \nabla_{\boldsymbol{R}_k} V_n(\boldsymbol{x}) + \sum_n \tilde{a}_n \\ &\quad \times \left\{ C_k^n \langle \nabla_{\boldsymbol{R}_k} k | \hat{H} - \epsilon_n | j \rangle C_j^n + C_i^n \langle i | \hat{H} - \epsilon_n | \nabla_{\boldsymbol{R}_k} k \rangle C_k^n \right\}. \end{aligned} \tag{10}$$

Here $\Phi_{\lambda_i}(|\boldsymbol{R}_k - \boldsymbol{R}_i|)$ is the net electrostatic potential at the nucleus of site k, $\boldsymbol{R}_k$, having nuclear charge Z_k, due to the nucleus and the site density $n_{\lambda_i}(\boldsymbol{x}_i)$ for site i. The first term in equation (10) therefore gives purely repulsive Hellman–Feynman-like pair forces. The second term arises because the trial density and output density do not coincide and can be rewritten

$$\int \mathrm{d}\boldsymbol{x}\ [n_{\mathrm{out}}(\boldsymbol{x}) - n(\boldsymbol{x})\nabla_{R_k} V_n(\boldsymbol{x}) \tag{11}$$

where

$$n_{\mathrm{out}}(\boldsymbol{x}) = \sum_n \bar{a}_n C_i^n C_j^n \langle i|\boldsymbol{x}\rangle\langle \boldsymbol{x}|j\rangle \tag{12}$$

is the output density from the solution of the Schrödinger equation. The density parameter forces in equation (9) can be written in similar form

$$\frac{\partial E}{\partial \lambda_k} = \int \mathrm{d}\boldsymbol{x}[n_{\mathrm{out}}(\boldsymbol{x}) - n(\boldsymbol{x})]\frac{\partial V_n(\boldsymbol{x})}{\partial \lambda_k} \tag{13}$$

which makes explicit the vanishing of these forces when the trial density and output density coincide. (A pointwise coincidence will not occur if $n(\boldsymbol{x})$ has the form in equation (4) and the vanishing of the λ forces is due to the equivalence of integrals, i.e. an optimization of the mismatch of the 'in' and 'out' densities.) The third term in equation (10) gives the Pulay forces, which express the dependence of the orbital basis on the nuclear positions.

These force formulae refer to an 'all-electron' calculation. In practice, it is advantageous to eliminate the cores either by use of a pseudopotential or via a frozen-core approximation. In the former case the pseudopotential replaces the nuclear potential and the above results hold with minor modifications. In the latter case, the functional in equation (2) must be converted into one for the valence density alone and the force formula (10) acquires additional terms that express the orthogonalization of the valence orbitals to the frozen-core orbitals. Details are given in appendix 1.

Maintenance of adiabaticity by dynamical propagation would normally be expected to gain in efficiency compared with direct maximization/minimization methods—steepest descent or conjugate gradient—the larger the number of variables involved. However, direct methods may be preferable if the time step needed to integrate the λ, α motion is considerably shorter than the natural time step dictated by the nuclear motion, or if the nuclear trajectories can be propagated over many time steps without upgrading λ and α. This is a matter of gaining experience with the application under study.

The advocacy of a scheme that requires solution of a matrix eigenvalue problem in each time step may seem retrograde as compared with the plane-wave method of CP. However, within an approach based on orbitals, some procedure must establish the orthogonality property required for fermions. In the CP method, this is achieved via constraints within the Lagrangian whose imposition involves essentially the same computational cost as a matrix diagonalization. The difference in the present scheme is that the matrix involved has rank equal to the number of basis functions whereas in the CP method this is the number of occupied orbitals. This disadvantage may be

compensated for by savings in the reduction in the number of dynamical variables that must be propagated and the possibility to use much larger time steps during progagation without significant departures from adiabaticity. Several methods have been proposed for circumventing computational steps that are manifestly non-linear in the system size (see, for example, Baroni and Gianozzi 1992). Such methods are certainly imperative in connection with very large systems, of which there are an infinite number. However, the number of potential MD applications that refer to systems of moderate size, where the ultimate scaling behaviour of the method is not a determining factor, is also essentially infinite. The CPU requirement of the present method will ordinarily be determined by the evaluation of the matrix elements and not the diagonalization of the matrix. Since the basis is localized, this step scales as N^3 for $N < M$ and NM^2 for $N > M$, where M is proportional to the number of basis functions per site times the number of neighbours for which the overlap is non-vanishing.

3. The basis: matrix element evaluation

As the above discussion makes clear, it is important that the representation of the solutions of the Schrödinger equation be kept as compact as possible. The 'fireball' basis introduced by Sankey and Niklewski (1989) where atomic orbitals are renormalized to vanish at a fixed radius is an ingenious choice and has the important advantage of truncating the Hamiltonian and overlap matrices drastically. The disadvantages are a lack of flexibility and possibility for systematic improvement and the use of numerical basis functions that limits the number of steps that can be taken analytically. We have chosen a more conventional route and use analytic functions that can be translated analytically for the purpose of integral evaluation. Gaussians obey the simplest translation theorems and suitable contracted Gaussian orbitals could be used in the present context. We have chosen instead to use exponential Λ-functions, as described in detail by Trivedi and Steinborn (1982),

$$\Lambda_{nL}(\alpha, \boldsymbol{R}) \equiv N_{nl}(\alpha) x^l L^{2l+2}_{n-l-1}[x] \mathrm{e}^{-x/2} Y_L(\hat{\boldsymbol{R}}) \tag{14}$$

where $x = 2\alpha|\boldsymbol{R}|$, $N_{nl}(\alpha)$ is a normalization constant, $L^l_n(X)$ an associated Laguerre polynomial and Y_L a spherical harmonic with label $L = l, m$. These functions form a *complete, orthonormal* set of site-localized functions and are linearly related to the set of Slater-type orbitals (STOs) (which is complete but not orthogonal). Their suitability within the present context devolves from the existence of a global ('one-range') expansion theorem of the form

$$\Lambda_{nL}(\alpha, \boldsymbol{r}_j) = \sum_{n'L'} S^{n'L'}_{nL}[\alpha, \boldsymbol{R}_{ji}] \Lambda_{n'L'}(\alpha, \boldsymbol{r}_i) \tag{15}$$

where the $S^{n'L'}_{nL}[\alpha, \boldsymbol{R}_{ji}]$ are structure constants depending on the translation vector, $\boldsymbol{R}_{ji} \equiv \boldsymbol{R}_j - \boldsymbol{R}_i$, between sites and $\boldsymbol{r}_i \equiv \boldsymbol{r} - \boldsymbol{R}_i$ is a point in space referred to the location of site i. Specifically, the structure constants are given by

$$S^{n'L'}_{nL}[\alpha, \boldsymbol{R}_{ji}] = \alpha^{-3/2} \sum_{n''L''} C^{nLn'L'}_{n''L''} \Lambda_{n''L''}(\alpha, \boldsymbol{R}_{ji}) \tag{16}$$

where the coefficients C are independent of the atom locations. Unlike analogous expansions for other localized functions, which display pronounced oscillations, the Λ-function expansion has excellent pointwise convergence properties, allowing two-centre integrals to be reduced to a relatively small number of one-centre integrals. All overlap elements and matrix elements of the kinetic energy taken with the Λ-functions or their derivatives can be performed efficiently with the aid of the expansion theorems, as detailed in appendix 2.

The remaining matrix elements that must be calculated involve the Coulomb and exchange–correlation potentials, which we consider separately. Since the trial density is a sum over site densities, the associated Coulomb potential is also a sum over sites,

$$\phi(\boldsymbol{x}) + V_{\text{ext}}(\boldsymbol{x}) = \sum_i \Phi_{\lambda_i}(\boldsymbol{x}_i) \tag{17}$$

so the required matrix elements can be written as sums of two- and three-centre integrals, e.g.

$$\langle i|\phi(\boldsymbol{x}) + V_{\text{ext}}(\boldsymbol{x})|j\rangle = \sum_k \langle i|\Phi_{\lambda_k}(\boldsymbol{x}_k)|j\rangle \tag{18}$$

with the k-sum running over sites i and j and neighbouring sites. All integrals are then converted to sums of one-centre integrals using the expansion theorems to translate i to j, j to i, or i and j to k. Since the site potentials are spherically symmetric, the resulting integrals are one-dimensional and the sums of structure constants involved are correspondingly truncated. In addition, all singularities in the potential occur at the origin of coordinates and are taken care of by the volume element. Details with regard to three-centre integrals are given in appendix 3.

Matrix elements of the exchange–correlation potential, e.g. $\langle i|\mu_{\text{xc}}|j\rangle$, offer the most resistance to efficient computation because $\mu_{\text{xc}}(\boldsymbol{x})$ behaves like $[\sum_i n_{\lambda_i}(\boldsymbol{x}_i)]^{1/3}$ and cannot be written exactly as a sum over sites. Sankey and Niklewski (1989) found an approximation procedure that seems to be relatively accurate but may fail if low densities at a bond centre are encountered. We believe that an alternative method will prove more accurate in general. This is similar in spirit to a procedure suggested by Jones (1988) and involves fitting the functional dependence of $\epsilon_{\text{xc}}(n)$ and $\mu_{\text{xc}}(n)$ to a polynomial in n,

$$\epsilon_{\text{xc}}[n] = a_0 + a_1 n + a_2 n^2 + \cdots \qquad \mu_{\text{xc}}[n] = a_0 + 2a_1 n + 3a_2 n^2 + \cdots. \tag{19}$$

The property $\mu_{\text{xc}} = \mathrm{d}[n\epsilon_{\text{xc}}]/\mathrm{d}n$ is preserved and the coefficients $a_0, a_1, \cdots$ should be chosen to optimize the density dependence of both ϵ_{xc} and μ_{xc}. It is advantageous to choose the coefficients so that the lower-order terms carry the main weight even if this results in a slightly worse fit than a free variation of the parameters. This is because matrix element contributions from the zeroth and first terms can be evaluated exactly while for higher-order terms approximations must be used. The series must be carried to at least quadratic order to guarantee a stable simulation and this was found to be adequate for hydrogen systems at not too large or small density. In general, higher-order terms will be necessary.

In conjunction with a sum over site density and a polynomial approximation, matrix elements of μ_{xc} involve sums of multi-centre integrals. These can be arranged (roughly) as a power series in the overlap of orbitals centred on adjacent sites and

evaluated at several levels of approximation. The simplest level, which we expect to be adequate in general, involves at worst three-centre integrals of the same form as those which contribute to the electrostatic matrix elements. Higher-order terms can be included if necessary via factorization formulae whose accuracy improves the larger the contribution made. Details are given in appendix 4. The use of an approximation for the exchange–correlation matrix elements was anticipated in the force formulae in equations (9) and (10), which remain exact derivatives of the energy expression in equation (6) *whatever approximations* are made for the matrix elements (provided only that these are made consistently in energy and force). The only consequence of matrix element approximations is that the λ forces determining the motion of the density parameters do not vanish exactly at the point where $n_{\text{out}}(\boldsymbol{x}) = n(\boldsymbol{x})$.

The evaluation of the energy in equation (6) is greatly facilitated by the spherical symmetry of the site densities and their associated Coulomb potentials. For H and first-row elements, a site-density representation in terms of Λ-functions is sufficiently accurate and the electrostatic energy then can be calculated analytically. If numerical site densities are used, one-dimensional one-centre and two-dimensional two-centre integrals must be performed by numerical quadrature, e.g. in elliptic coordinates. The exchange–correlation energy requires a sum of three-dimensional integrals with integrands $n_{\lambda_k}(\boldsymbol{x}_k)(\mu_{\text{xc}}[n] - \epsilon_{\text{xc}}[n])$, which can be treated in a similar way as the corresponding Hamiltonian matrix elements calculation. The energy need not be calculated in every time step so its evaluation contributes negligibly to the CPU cost of a simulation, which is determined primarily by the three-centre integrals that contribute to the Hamiltonian matrix and to the Pulay forces in equation (10). Evaluation of the Pulay forces is a difficult step in all localized-basis schemes. In the present scheme, crucial advantage accrues from the expansion theorems obeyed by the Λ-functions. Matrix elements contributing to the Pulay forces involve the gradients of the basis functions and can be evaluated using the expansion formulae,

$$\nabla_{\boldsymbol{R}_j} \Lambda_{nL}(\alpha, \mathbf{r}_j) = \sum_{n'L'} \left\{ \nabla_{\boldsymbol{R}_j} S_{nL}^{n'L'}[\alpha, \boldsymbol{R}_{ji}] \right\} \Lambda_{n'L'}(\alpha, \mathbf{r}_i). \tag{20}$$

This means that the Hamiltonian and Pulay matrix elements are evaluated in parallel, which combines calculational efficiency with maintenance of strictly equivalent numerical errors due to truncation of the expansion series.

4. Discussion of basis adequacy

The accuracy of the nuclear forces in equation (10) as compared with the derivatives of the exact Kohn–Sham energy depends on the adequacy of the orbital basis of Λ-functions together with the density representation in equation (4). Since Λ-functions are basically STOs, the number required to attain basis convergence is well known and our experience confirms that two functions per atomic orbital ('double zeta') are necessary and sufficient. The consequences of a sum over sites approximation for the density in conjunction with the functional in equation (2) are less clear *a priori*, and remain to be established. There is considerable evidence that this is a much better approximation than it might appear. Correspondence with full Kohn–Sham calculations for selected dimers (Harris 1985), bulk solids (Polatoglou and Methfessel 1988, 1990) and surfaces and vacancies (Finnis 1990), was quite favourable. Since the

actual ground-state density of any chemically interacting system must deviate quite markedly from a sum of spherically symmetric atom-centred site densities, this can be taken as an indication that the density functional in equation (2) is quite flat about its stationary point. The reason has been discussed in terms of the expression for the curvature of $E[n]$ in terms of the trial density ('in') and the 'out' density given by the Schrödinger equation (Finnis 1990) and is related to the inherent instability of the self-consistency cycle whereby the Kohn–Sham equations are usually solved. This instability is apparent at the atomic level. If the start density used to construct the initial trial potential for the atom is somewhat too contracted with respect to the correct atom density, the nuclear potential will be too strongly screened and the 'out' density will 'overshoot' and be much too expanded. If this is used as an 'in' density, the next 'out' density will be far too contracted, and so on. Stable iterations result only if this oscillation is damped out by feeding back only a small fraction of the 'out' density in each iteration. 'Overshooting' magnifies the error made if the Kohn–Sham functional is evaluated on a 'one-pass' basis using a potential constructed from some assumed start density, but does not occur in connection with the density functional in equation (2), where the Coulomb potential used in energy and force evaluation is that due to the trial density itself and not to the 'out' density from the Schrödinger equation . This is the reason why equation (2) gives a reasonably accurate energy in conjunction with a trial density that may be quite far from the correct density and which, if used in a 'one-pass' evaluation of the Kohn–Sham functional, may lead to unacceptable error.

The kind of accuracy that can be achieved with a sum over spherically symmetric site densities in systems displaying different bonding characteristics is illustrated in table 1, where we show calculations of spectroscopic parameters of the first-row dimers Li_2 to F_2. These are compared with standard Kohn–Sham calculations and with measured values. The column marked PA gives the results of Painter and Averill (1982), obtained via direct minimization of the Kohn–Sham functional, equation (1), using an extensive Gaussian orbital basis. Since the stationary points of the Kohn–Sham functional are formally identical to those of equation (2), differences between the two sets of theoretical results can be attributed to orbital or the density basis error (or both) in equation (6), or to non-convergence of the Gaussian orbital basis of PA. The experimental values in table 1 are those quoted by PA and are included to give a measure of the overall accuracy that can be achieved in LDA calculations (and so the level of accuracy it makes sense to aim at in the theory).

Table 1. Spectroscopic parameters of first-row dimers. Comparison of present results with Painter and Averill (1982) and with experimental values.

Dimer	E_b (eV)			R_e (au)			ω_e (meV)		
	Equation (6)	PA	Exp.	Equation (6)	PA	Exp.	Equation (6)	PA	Exp.
Li_2	1.32	1.01	1.03	5.24	5.12	5.05	43	43	44
Be_2	0.58	0.50	0.10	4.65	4.63	4.71	45	44	36
B_2	4.12	3.93	2.90	3.04	3.03	3.04	133	134	130
C_2	8.00	7.19	6.20	2.34	2.36	2.35	240	232	230
N_2	11.52	11.34	9.91	2.08	2.08	2.07	288	296	292
O_2	7.77	7.54	5.20	2.35	2.31	2.28	191	194	196
F_2	4.09	3.32	1.65	2.68	2.62	2.68	132	133	111

The results marked 'equation (6)' in table 1 were obtained with the use of an orbital basis consisting of two functions per atomic orbital ('double zeta') plus 'polarization functions' ('atom unoccupied' p or d functions) and are essentially orbital basis converged (by which is meant that selected control calculations using further orbitals changed the binding energy by < 0.1 eV). The polarization functions included in the basis influenced results most strongly for Li_2 and Be_2, which we discuss below. In other cases, the energy shifted downwards almost rigidly by a small amount (e.g. $\sim$ 0.4, 0.7, 0.4 eV for C_2–O_2). The density was constructed as in equation (4) with the site density represented by two exponentials, one each for the core and valence densities. The exponents were determined via the maximum property of the density functional in equation (6), which was found to be very well fulfilled in all cases. Comparison with independent, purely numerical atom calculations using the Kohn–Sham functional showed that atom energies calculated with equation (6) and the basis indicated above were given to better than 0.1 eV (i.e. $\sim$0.005%). This shows that a representation of the atom densities as the the sum of two Λ-functions gives negligible error in the atom's energy so that the main source of error in the dimer calculations devolves from restrictions on the trial density that arise because of the form of equation (4). (A spherically symmetric site density is inherently restrictive for the dimer but not for a central-field atom.) Assuming PA's results are well converged in orbital basis, the differences between the results in the first two columns of table 1 reflect inaccuracies in the density representation. Since these would be expected to yield too low a dimer energy, the binding energies found in the present calculations should be larger than those of PA, which is a consistent trend.

In general, correspondence with PA's equilibrium separations and vibration frequencies is excellent. This indicates that the energy balance within dimer bonds with bond orders ranging from 0 (Be_2) to 3 (N_2), and π as well as σ character, is described almost perfectly in all cases, despite the spherical site densities used in equation (6). The present results for C_2, N_2 and F_2 are significantly closer to the results of PA than earlier results obtained using unmodified atom densities as site density in equation (4) and an orbital basis of muffin-tin orbitals (MTOs) (Harris 1985). Since the present calculations gave lower binding energies, the systematically improved agreement with PA's equilibrium separations and vibration frequencies is due more to an improvement in orbital basis on going from MTOs to Λ-functions than to flexibility in the density basis. The comparison of theoretical and experimental R_e and ω_e in table 1 shows that the use of a simple density respresentation in conjunction with equation (6) does not imply any significant loss of accuracy as compared with a full solution of the Kohn–Sham equations with regard to intramolecular properties.

Limitations of the density representation are apparent, however, in the binding energies. Significant differences with PA are apparent for Li_2, F_2 and C_2. In the case of C_2 we find a more strongly bound molecule with a slightly smaller equilibrium separation and stiffer force constant. This may be due in part to inaccuracy of the density basis for the π^4 ground state, but could also suggest that PA's Gaussian basis calculation may not be quite converged in this case. Li_2 and F_2 are more clear-cut. Here, the too large binding energy is associated with a bond that is longer than PA's, and with a difference that is significantly larger than is typical ($\sim$0.1 au compared with a typical 0.02 au). It is unlikely that these concomitant discrepancies can be due to orbital basis inadequacies (in either calculation) and we believe they reflect limitations in our density basis. It is striking that the largest discrepancy in E_b by far, a 30% difference, is for the simplest dimer, Li_2, while the smallest is for the triple

$\pi\sigma$ bond of N_2, whose density one might have thought would be hardest to represent with a simple site sum. In fact, a sum of atom-centred spherically symmetric site densities can describe a charge build-up at the bond centre that is controllable to some extent through the range of the site densities. What cannot be described is a *polarization* of the dimer density in the region close to the nuclei. Such polarization effects occur for all dimers, but are particularly large in the case of Li_2, for which the inclusion of p polarization functions in the orbital basis lowers the binding energy by ~ 0.4 eV, or 40%. An equivalent figure for H_2 would be ~ 0.05 eV, or 1%, and the difference reflects the readiness of the Li atomic potential to support a 2p level (cf. the reason why Be_2 is not a Van der Waals dimer). Results for the bond of F_2 differ from those of PA in the same way as for Li_2, presumably for the same reason.

As pointed out in section 2, the trial density can take account of intra-atomic density polarization if p contribtions on each site are included, or by use of appropriately located 'empty-site' densities. Errors arising from this effect cannot, however, be 'traded off' by linking the inability of the trial density to polarize to a concomitant limitation in the orbital basis. This gives an energy change of opposite sign, but the two basis errors are insufficiently closely coupled to give a systematic cancellation. In practice, the error in the intramolecular properties R_e and ω_e (and so the forces operating in the molecular state) became systematically smaller the more extensive the orbital basis, regardless of the absolute value of the energy. This suggests that the restrictions devolving from the use of equation (4) for the trial density will turn out to be relatively minor within any local minimum of the energy surface, but may be important with regard to the difference in energy between local minima that correspond to radically different bonding situations. In fact, such differences are in any event given rather poorly by the LDA, as is clear in table 1. With the exception of Li_2, the difference between the theoretical values of the binding energy is less than the differences between either and measured values. In recent years, LDA correction procedures involving gradients of the density (e.g. Perdew 1986, Becke 1991) have been proposed that appear to improve absolute energies systematically and substantially. Such corrections can be very easily built into the present scheme because of the simplicity of the density representation. This remains true even if p wave site density contributions are necessary.

The results shown in table 1 refer to all-electron calculations, but very similar parameters were obtained within the frozen-core formulation (appendix 1). For example, the largest difference in binding energy was for N_2, where the frozen-core approximation gave 11.29 eV as compared with the 11.52 eV in the all-electron case. In frozen-core calculations, the core orbital was represented by a single Λ-function and valence-core orthogonality treated as detailed in equation (A1.2). The basis used to describe the valence orbitals could then be taken to have one less 1s Λ-function than for the all-electron case. Both frozen-core functionals, equations (A1.1) and (A1.4), gave very similar results, indicating that a complete decoupling of valence and core as in equation (A1.4) involves negligible error. This is advantageous with regard to exchange–correlation matrix element evaluation because the valence charge density is much smaller than the total density so that the series in equation (19) can be truncated in lower order.

5. Molecular dynamics simulations for hydrogen clusters

In previous work (Harris and Hohl 1990) the MD features implied by equations (7)–

(10) were illustrated for the vibrations of a single H_2 molecule. We now extend this work to treat clusters of hydrogen atoms with 16 and 128 atoms. These calculations represent the first steps in a systematic application of the method to the structure and dynamics of hydrogen under pressure. The results of this study will be reported elsewhere and our aim here in presenting preliminary data is just to illustrate how our MD scheme works in practice. The protons will be treated as classical particles and no attempt will be made to account for the influence quantum proton dynamics may have on behaviour.

For hydrogen systems, the site densities in equation (4) can be taken to be single exponentials,

$$n_{\lambda_i}(\boldsymbol{x}) = \frac{\lambda_i^3}{8\pi} \exp(-\lambda_i |\boldsymbol{x} - \boldsymbol{R}_i|) \tag{21}$$

which obey the 1s Λ-function translation theorem. The λ_i were allowed to vary with site but no account was taken of charge-transfer effects. A quadratic approximation for the exchange–correlation energy and potential was used (equation (19)) with parameters $a_0, a_1, a_2 = -0.185, -2.25, 3.25$ au. This gave an adequate description of the H_2 binding energy curve over a region of energy spanning ~ 3 eV from the minimum. Four-centre integrals then contribute to matrix elements of the exchange–correlation potential and these were not always negligible because bond lengths can be quite short in high-density hydrogen. Such contributions were found to be estimated rather accurately by formulae like equation (A4.5). All three-centre integrals encounted in the Hamiltonian, the orbital exponent force and Pulay force were evaluated using the translation theorems. An orbital basis consisting of one single 1s Λ-function per atom was used throughout. Including 2s and 2p functions was found to influence the energy of H_2 essentially via a rigid shift of about 0.05 eV, implying a negligible force correction. This was confirmed in dynamical simulations for H_8 and H_{16} using one and five basis functions per atom. Differences were marginal and no larger than would arise for example on using different LDA variants. Box boundary conditions were used with the system confined by repulsive one-particle potentials acting on the nuclei. The functional form of the confining potential was taken to be $(|X| - X_b)^2 \exp[\gamma(|X| - X_b)]$ for $|X| > X_b$ and zero otherwise. Here X is the x coordinate of a nucleus. Analogous potentials were applied with respect to the y and z coordinates. The box is characterized by its 'free volume' $V_f = 8X_bY_bZ_b$ or equivalently the corresponding r_s value defined by $V_f = 4\pi N r_s^3/3$, where N is the number of atoms. V_f is somewhat smaller than the actual volume available to the atoms because the walls are not infinitely steep and the boundary conditions correspond more nearly to constant pressure than to constant volume. Such boundary conditions are natural in cluster calculations using a localized basis, and are the most appropriate in connection with free clusters bound by chemical forces, where the boundaries are needed only to prevent evaporation during the initial annealing of the cluster to a configuration of low total energy. In the case of hydrogen clusters, the walls serve to confine the particles and simulate an external pressure. Periodic boundary conditions would be more appropriate to the behaviour of bulk hydrogen because they give rise to less pronounced surface and size effects. However, the behaviour of a finite number of hydrogen atoms confined by walls is interesting in its own right and yields useful, complementary information.

The cluster calculations proceeded by first placing the atoms in an assumed (cubic) crystal structure and allowing the system to relax to a nearby local minimum. This was

done in the simplest possible way via Newtonian dynamics using the Verlet algorithm with the proton velocities set to zero after each time step. The result of this procedure is shown for an H_{16} cluster in figure 1(*a*). The cluster formed a distorted structure comprising four squares on top of one another. The side lengths were $a_{in} = 2.18$ au and $a_{out} = 2.52$ au for the inner and outer squares. The inner squares were $d_{in} = 2.23$ au apart and the inner and outer squares were separated by $d_{out} = 3.91$ au. This structure corresponded to a stable local minimum of the energy with respect to the above lengths. An H_8 cluster constrained to a cube was found to adopt a side length of 2.22 au so the H_{16} structure is basically one H_8 cube in the centre with two H_4 squares in the outer layers.

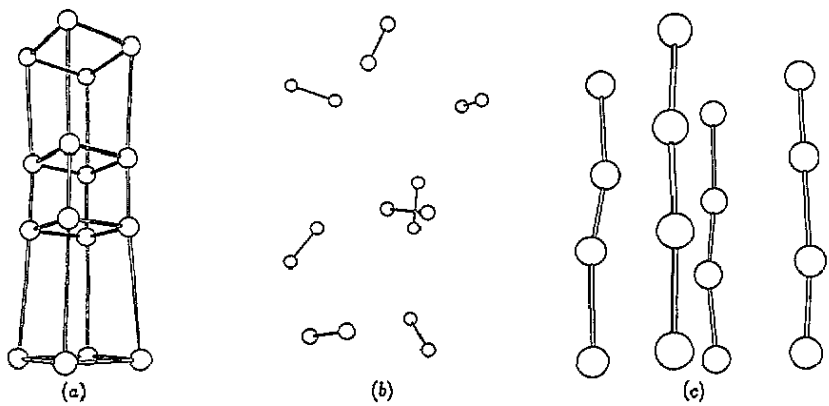

Figure 1. Typical configurations of an H_{16} cluster confined by walls. (*a*) Local minimum closest to a cubic structure. (*b*), (*c*) Snapshots of simulation at $T = 3300$ K and nominal $r_s = 1.5$ (*b*), 0.6 (*c*).

Starting from this local minimum the H_{16} cluster was heated to a very high temperature (~16 000 K) and the box dimensions were gradually reduced until the free volume corresponded to $r_s = 1.5$ (wall dimensions $X_p = Y_p = Z_p/2 = 4.84$ au). The system was then quenched down to a temperature of ~3000 K, corresponding to a mean classical kinetic energy of roughly the zero-point energy of the proton motion. After equilibration for a few thousand time steps, statistics were collected over a further 5000 time steps. The masses chosen for the orbital exponents and site density parameters α_i, λ_i in the Lagrangian, equation (7), were 220 and 160 au, respectively. This choice gave a maximum kinetic energy of the $\alpha - \lambda$ system of 2×10^{-3} au indicating that the propagation proceeded close to electronic adiabaticity. It was found possible to propagate with a time step of $\Delta = 20$ au, which is very much larger than would be possible in plane-wave methods with such rapid nuclear motion. This advantage accrues because the auxiliary variables that are propagated along with the nuclear positions are merely exponents and change relatively slowly with time whilst in the CP method plane-wave coefficients are propagated that change rapidly with time. The simulation was run in principle microcanonically but a small heating effect arose because particles at the walls propagated slightly into the classically forbidden region and tended to reflect with a too large energy (a consequence of the large time step). The heating effect was controlled by setting an upper limit for the kinetic energy of a reflected particle (five times the mean thermal energy of the

system). On the rare occasions this limit was exceeded, the particle's speed was cut down by 30%. The average temperature for the simulation was $\bar{T} = 3300$ K, with RMS temperature fluctuation

$$\Delta T \equiv \sqrt{\langle T^2 \rangle_t - \bar{T}^2} \sim 450 \text{ K}.$$

The box dimension and interparticle separations were then scaled down to correspond to a higher density of $r_s = 1.1$ and re-equilibrated at 3000 K for several thousand time steps. Statistics were then collected for a further 5000 time steps. This procedure was then repeated for $r_s = 0.9$ and $r_s = 0.6$. At the very highest density, $r_s = 0.6$, the dynamical fluctuations were fast and it was found necessary to reduce the time step to $\Delta = 10$ au.

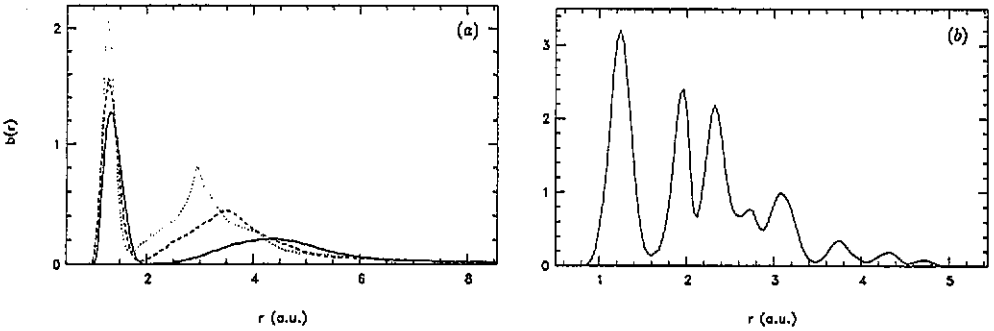

Figure 2. Interatomic distance distribution, $b(r)$, of H_{16}. (*a*) $r_s = 1.5$ (full curve), $r_s = 1.1$ (broken curve), $r_s = 0.9$ (dotted curve). (*b*) The same for $r_s = 0.6$.

Some data from these simulations are displayed in figures 1 and 2. Figure 1(*b*) shows a snapshot of particle positions at the lowest density, $r_s = 1.5$, and illustrates that a molecular 'phase' forms at this density. The atoms formed molecules immediately during the initial anneal and these remained quite rigid throughout the subsequent simulation, indicating that the molecular 'phase' is very stable at this density. The mean bond length was 1.44 au, identical to that of the isolated molecule, with an RMS fluctuation of 0.16 au. A tendency of the molecular bond axes for neighbouring molecules to orient mutually at right angles was noticeable (one such case is apparent in the snapshot in figure 1(*b*)). The full curve in figure 2(*a*) shows the bond distance distribution, $b(r)$, defined such that $4\pi r^2 b(r)\mathrm{d}r$ gives the average number of particles whose distance from a given particle is between r and $r + \mathrm{d}r$. The distribution displays a sharp first peak at $r = 1.44$ au that integrates to unity, the coordination of the molecular phase, and is well separated from a broad feature centred at $r = 4.8$ au that arises from atoms in different molecules. The distributions of intermolecular distances (not shown) display features that can be identified with the shorter and longer box dimension, indicative of repulsive interactions between the molecules. As the density increases, the intermolecular repulsion strengthens, the particles are squeezed closer to the walls and features in the distance distributions sharpen correspondingly. The leading peak in $b(r)$ sharpens considerably and shifts slightly inwards implying a shortening of the bond length with increasing density. This is evident in figure 2(*a*), where the full, broken and dotted curves refer to

$r_s = 1.5, 1.1$ and 0.9 respectively. The mean bond length was found to be 1.38 and 1.34 au with mean square fluctuations of 0.15 and 0.13 au at $r_s = 1.1$ and 0.9, respectively. A similar behaviour was found by Ceperley and Alder (1987) in their quantum Monte Carlo study of the molecular phase of bulk hydrogen. On further increase of the H_{16} density, to a nominal $r_s = 0.6$, a distance distribution is found (figure 2(*b*)) that is quite different from those at lower density. The first peak is again very clearly defined, but the coordination is now 1.5 rather than 1. The reason for this is evident in figure 1(*c*), which shows a snapshot of the atomic positions. The atoms have arranged themselves not in a close-packed structure, as one might have expected at such high density, but in four chains of four atoms each with short and longer distances within and between the chains. The two outer atoms in a chain have coordination 1, the inner ones coordination 2, accounting for the observed average coordination of 1.5. The chains are very stable, as is clear from the sharp-peaked structure of $b(r)$. This was particularly evident in a dynamical visualization. Thermally induced buckling was observed to heal very quickly and on no occasion was transfer of atoms between chains observed. The chains were strongly repelling and were held in place by the walls of the cell. The mean bond length within the chains was 1.26 au with RMS fluctuation 0.11 au. The distance between the inner atoms in a chain was slightly shorter than for the outer atoms. Interestingly, a detailed theoretical study of metallic hydrogen under pressure (Brovman *et al* 1972) predicted that filaments arranged on triangular or square lattices should be preferred at lower pressure, with compact structures gaining stability only at very high pressure. Recent work (Barbee *et al* 1989, Hohl *et al* 1992) has shown also a tendency towards chain formation and filamentary structure, in broad agreement with the earlier study. The chain structure we find for H_{16} may be a feature of the rectangular pressure cell employed, but nevertheless was preferred to higher-coordination structures, such as in figure 1(*a*). This suggests that filament formation in hydrogen systems is a result of local chemical effects rather than long-range forces.

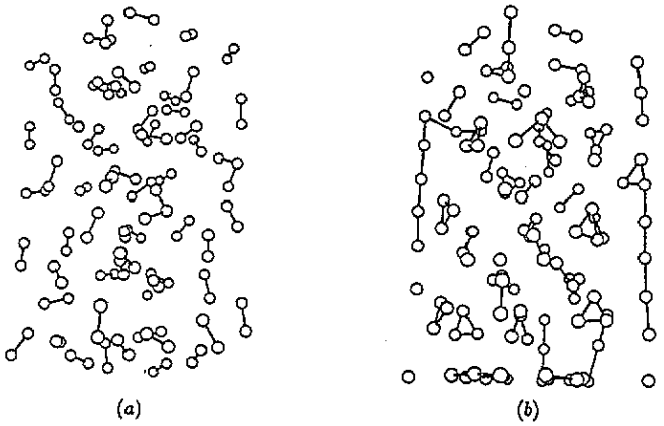

Figure 3. Snapshot of a simulation of an H_{128} cluster confined by walls at $T = 3000$ K and (*a*) $r_s = 1.5$, (*b*) $r_s = 1.1$.

For H_{16}, all atoms are on the surface of the cluster and the behaviour is strongly influenced by the particle–wall interaction. Figures 3 and 4 show some preliminary

data for a cluster with 128 atoms where the interparticle interaction is relatively more important. The cluster was prepared as for H_{16}, annealed and cooled to $T \sim 3000$ K. After equilibration, statistics were compiled for 2000 further time steps at which time the distributions were found to be stable (in fact, distributions changed little beyond 500 time steps). The temperature remained close to 3000 K with mean square fluctuation $\Delta T \sim 210$ K. Figure 3 shows snapshots of the particle positions for nominal densities $r_s = 1.5$ and 1.1. At the smaller density, the state is clearly molecular and virtually all the H atoms are bound in pairs (the criterion for drawing in a bond is that the distance between two atoms should be < 1.9 au). The bond distance distribution, $b(r)$, shown in figure 4(*a*), is similar to that found for H_{16}, displaying a broad maximum centred about the intramolecular distance, but the leading peak is broader than one would expect on the basis of the gas-phase pair interaction between hydrogen atoms. The mean bond length is 1.42 au with RMS fluctuation 0.23 au. This is qualitatively consistent with the strongly modified pair interaction found by Ceperley and Alder (1987) for the molecular phase of hydrogen under pressure, and with the experimental observation of a softened vibron with increasing density (Hemley and Mao 1988, Lorenzana *et al* 1989). The weak feature at $r \sim 3.8$ au reflects the distance distribution for atoms in different molecules. The intermolecular distance is slightly smaller than for H_{16} because the larger system has a smaller surface-to-volume ratio and so is more dense at the same nominal r_s.

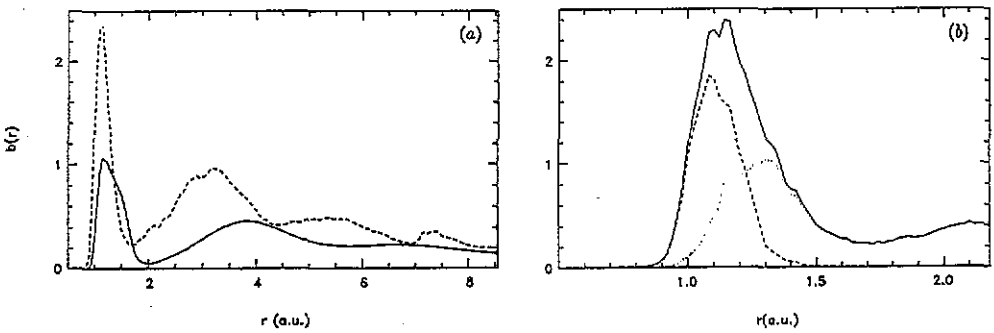

Figure 4. Interatomic distance distribution, $b(r)$, of H_{128}. (*a*) $r_s = 1.5$ (full curve), $r_s = 1.1$ (broken curve). (*b*) Leading peak for $r_s = 1.1$. The broken curve gives the contribution of triangles, the dotted curve all other microstructures.

The molecular 'phase' of H_{16} persists to high nominal density and at $r_s = 1.1$ all atoms remained paired, with no detectable bond breaking. This is not the case for the larger cluster, as is clear in the snapshot shown in figure 3(*b*), which is typical for the simulation. A rich variety of microstructures is observed, singles, pairs, triads and chains that remained intact for relatively long times at the simulation temperature of 3000 K. Unsurprisingly, the bond-distance distribution, $b(r)$ (figure 4(*b*)), does not fall to zero between first- and second-nearest-neighbour peaks. Integrating the leading peak up to the first minimum gives 1.25, showing that, although the state is clearly not molecular, a low coordination is preferred, as for H_{16} at $r_s = 0.6$. The leading peak includes contributions from several microstructures and is characterized by a substantial number of very short bonds that were not found in the H_{16} simulations. The origin of the short bonds is evident in figure 4(*b*), where we show the relative

contribution of triangular (broken curve) and other (dotted curve) microstructures to the leading peak in $b(r)$. (A triangular structure was declared if a single H atom bonded to two neighbours with bond distances of less than 1.3 au, and the largest angle in the triangle thus formed was less than 90°.) As the snapshot in figure 3(*b*) illustrates, triangles were very prevalent in the simulation, amounting to 43% of all bonds contributing to the leading peak, and were responsible for practically all the short bonds. Short bonds were found also in Ceperley and Alder's (1987) quantum Monte Carlo simulations for the (unstable) molecular phase of hydrogen at high density, but appear to have been absent in a standard Car–Parrinello simulation using 64 atoms and periodic boundary conditions (Hohl *et al* 1992). Chain structures were observed in this simulation, and are common in the cluster simulation, preferentially lining the walls. Alignment of these chains across the walls is responsible for the rather sharp edge in $b(r)$ at $r \sim 7.2$ au, which is close to the smaller wall dimension. A complex microstructure in the H_{128} cluster is perhaps to be expected in view of the finding of Brovman *et al* (1972) that many quite different structures of bulk hydrogen lie close in energy. However, it is possible that the structural features we find are strongly influenced by charging effects that cannot be tracked properly using a trial density that displays local charge neutrality. This point is currently under investigation.

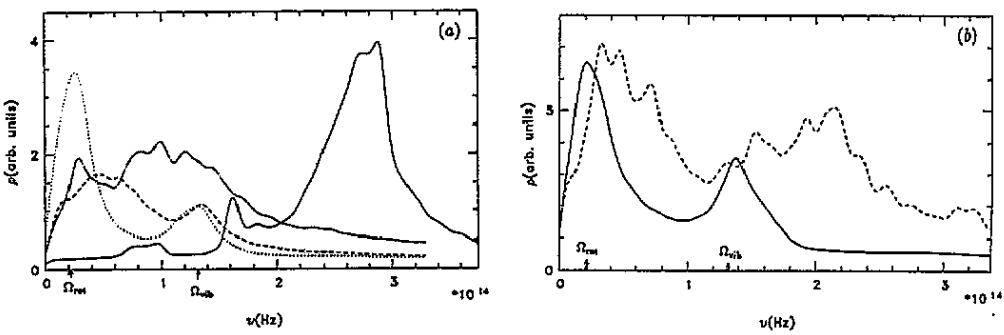

Figure 5. Fourier transform of velocity autocorrelation function: (*a*) H_{16} for nominal $r_s = 0.6$ (full curve), 0.9 (chain curve), 1.1 (broken curve), 1.5 (dotted curve); (*b*) H_{128} for nominal $r_s = 1.1$ (broken curve), 1.5 (full curve).

Dynamical information from the simulations is shown in figure 5 where the spectral density

$$g(\omega) = \frac{1}{T}\int_0^T g(t)\ \cos(\omega t)W(t)\ \mathrm{d}t \tag{22}$$

is plotted against frequency, ω. Here, $g(t)$ is the velocity autocorrelation function

$$g(t) = \sum_{i=1}^{N} \frac{\langle v_i(t)\cdot v_i(0)\rangle}{\langle v_i(0)\cdot v_i(0)\rangle} \tag{23}$$

where the sum runs over all atoms, i, of total number N. The ensemble average is defined by

$$\langle v(t_n)\cdot v(0)\rangle = \frac{1}{N_t - n + 1}\sum_{m=0}^{N_t-n} v(t_{n+m})\cdot v(t_m) \tag{24}$$

where N_t is the number of time steps with $t_n = n\Delta t$. The window function $W(t) = \cos(\pi t/2T)$ suppresses finite-time sampling oscillations. Additional damping of oscillations due to noise was achieved by broadening the spectra using a Gaussian of width ~ 50 cm^{-1}. Spectra for H_{16} are shown in figure 5(*a*). At the lowest density, $r_s = 1.5$, two features are evident at low and high energy and due respectively to rotations and to intramolecular vibrations, as exemplified by the frequencies Ω_{vib} and Ω_{rot} that are marked on the figure. The former is the classical vibration frequency of a hydrogen molecule, the latter is the rotation frequency of an H_2 unit having thermal energy. As the density increases the confinement of the particles inhibits transport and quenches rotational motion. The rotational peak then broadens and shifts upwards in frequency due to the 'confinement' of the rotational coordinate of one H_2 unit via its interactions with other units (i.e. the rotational motion tends to become 'librational'). At the higher density of $r_s = 0.9$ the vibrations and librations mix strongly to form a broad band of frequencies. Finally, below the transition to the atomic 'chain phase', all resemblance to the free molecular spectrum is lost and two new peaks appear, at ~ 2.8 and 1.8×10^{14} Hz, respectively. The high-frequency peak is due to 'buckling' vibrations and is indicative of the strong interchain and chain–wall repulsion. The lower-frequency peak is due to intrachain vibrations. The spectral density for the low-density H_{128} simulation (figure 5(*b*)) is quite similar to that found for H_{16} and symptomatic of a molecular phase. Unsurprisingly in view of the rich variety of microstructures found, the higher density spectrum displays no readily identifiable features.

6. Summary and concluding remarks

In this paper we have presented a method for carrying out molecular-dynamics calculations in systems with chemical interactions. The method is similar in spirit to the method of Car and Parrinello (1985), but differs in two respects. Forces are drawn from a functional that has the same stationary points as the Kohn–Sham functional, but is defined on function space. This allows the use of simple, approximate representations for the density, such as sums over spherically symmetric site densities. The one-particle Schrödinger equation is solved using an LCAO orbital basis of Λ-functions closely related to STOs. These functions obey a global translation theorem, enabling multi-centre integrals to be reduced to manageable numbers of single-centre integrals. Exponents in the orbital and density basis were optimized dynamically. The elements of the method were examined in connection with hydrogen clusters and first-row dimers. For hydrogen, an orbital and a density basis consisting of a single exponential per atom were found sufficiently accurate. Through the first row, an orbital basis of 'double zeta' quality (two Λ-functions per atom-occupied atomic orbital), and a density basis consisting of two exponentials, one each for core and valence, was found adequate. All-electron and frozen-core versions of the method were found to give very similar results.

Explicit simulations for H_{16} and H_{128} illustrated how our MD scheme works in practice and gave valuable information on dynamical aspects, such as choice of appropriate masses for the auxiliary variables. It was found that mass ratios chosen in small clusters to maintain adiabaticity of the nuclear motion were transferrable to larger systems and propagation over long time periods was possible with negligible heating of the auxiliary system. Because the exponents vary only weakly with the

nuclear locations, stable, near-adiabatic propagation was possible using a time step dictated essentially by the rapidity of the nuclear motion. With appropriate choices for the auxiliary masses, a simulation with time step Δ was stable provided $\nu_{max}\Delta < 0.1$, where ν_{max} is the maximum frequency of the nuclear motion (cf. the spectra in figure 5). In general, we would expect the time step required for stable propagation to be much larger than in an equivalent Car–Parrinello calculation, where rapidly varying plane-wave coefficients are propagated dynamically. For atoms that can be treated with a small plave-wave cut-off, this advantage is more than off-set by a greater CPU requirement per time step because of the need to evaluate a large number of matrix elements and diagonalize a large matrix. The main advantage of a localized-orbital-based method is its ability to treat strong potentials. The hydrogen atom can be described adequately by a single 1s orbital, whereas a plane-wave cut-off of at least 36 Ryd is needed (Barbee *et al* 1989). For the central atoms of the first row even larger cut-offs are needed even when a pseudopotential is used. As we noted in section 4, within the present method it is easier to treat the dimers C_2–N_2 than Li_2. The converse is of course true with plane-wave-based methods.

Although our experience with actual simulations is limited currently to hydrogen clusters, there seems little doubt that the method will prove accurate and practicable for atoms through the first row, and probably throughout the periodic table. The CPU requirement is determined by the number of three-centre integrals that are needed in matrix element evaluation. This depends on the number of basis orbitals per atom, the range of the orbitals and the density of the system. A 'double zeta' orbital basis (two Λ-functions per atom-occupied atomic orbital) is required, but one exponent is large, limiting the number of overlaps and allowing orbital contractions if matrices become too unwieldy. A density basis of atom-centred, spherically symmetric site densities tends to give too large bond energies for bonds associated with a substantial intra-atomic density polarization. However, even in these cases, the forces acting in the bonding environment were well described. It would appear that fine tuning of the density basis is not necessary for most systems of interest. On invoking the frozen-core approximation, forces can be derived from a functional of the valence density only, for which a representation in terms of a single Λ-function per atom is adequate throughout the first row.

Appendix 1. Frozen-core approximation

The polarization of the atomic cores and concomitant back-polarization of valence orbitals has usually only a marginal influence on the interactions and can be neglected. This is done by invoking the frozen-core approximation whereby the core wavefunctions, $|c_i\rangle$, are assumed to maintain their atomic form throughout. The trial site densities in equation (4) are then sums of fixed core and variable valence densities, $n_t^i = n_c^i + n_{\lambda_i}^v$, and the sum over sites can be written $n_t = n_c + n_v$ where the core density of the system, n_c, varies only by rigid translations of the individual core densities as the atoms move. On substituting into equation (6) and making the additional assumption that the core densities on different sites do not overlap, the energy reduces to a function of the valence density and valence orbital exponents, λ_i, α_i,

$$E_v(\lambda_i, \alpha_i, R_i) = \sum_n^v \bar{a}_n C_i^n H_{ij} C_j^n - \int \mathrm{d}x\; n_v(x)\left\{\tfrac{1}{2}\phi_v(x) + \mu_{xc}[n_t(x)] - \epsilon_{xc}[n_t(x)]\right\}$$

$$+\int \mathrm{d}\boldsymbol{x}\; n_{\mathrm{c}}(\boldsymbol{x})\epsilon_{\mathrm{xc}}[n_{\mathrm{t}}(\boldsymbol{x})] + \tfrac{1}{2}\sum_{i\neq j}\frac{Z_{\mathrm{v}}^{i}Z_{\mathrm{v}}^{j}}{|\boldsymbol{R}_i-\boldsymbol{R}_j|} \tag{A1.1}$$

where the sum of eigenvalues runs over only the valence shell, $\phi_{\mathrm{v}}(\boldsymbol{x})$ is the Coulomb potential corresponding to the valence density, and Z_{v}^{i} the net charge of the ith core. The Hamiltonian and overlap matrix elements between valence orbitals, $|v_i\rangle$, must be corrected to incorporate the orthogonality of these orbitals to the cores,

$$H_{ij} \rightarrow H_{ij}^{\mathrm{v}} - \sum_{k}\epsilon_{\mathrm{c}}^{k}S_{ik}S_{kj} \qquad O_{ij} \rightarrow O_{ij}^{\mathrm{v}} - \sum_{k}S_{ik}S_{kj} \tag{A1.2}$$

where H_{ij}^{v} and O_{ij}^{v} are matrix elements taken with the unorthogonalized valence orbitals, $\epsilon_{\mathrm{c}}^{k}$ are the atomic core eigenvalues and $S_{ik}\equiv\langle v_i|c_k\rangle$. With these definitions the λ and α forces are given by the same formulae as for the all-electron case (equation (9)), and the forces governing the motion of the nuclear coordinates can be written

$$\begin{aligned}\nabla_{R_k}E_{\mathrm{v}}(\lambda_i,\alpha_i,\boldsymbol{R}_i) = {}& \sum_{n}^{\mathrm{v}}\tilde{a}_n C_i^n\Big\{\nabla_{R_k}\big[H_{ij}-\epsilon_n O_{ij}\big]\Big\}C_j^n \\ & + \nabla_{R_k}\sum_{i\neq k}\Big\{\frac{Z_{\mathrm{v}}^{i}Z_{\mathrm{v}}^{k}}{|\boldsymbol{R}_i-\boldsymbol{R}_k|} - \int \mathrm{d}\boldsymbol{x}\; n_{\lambda_i}^{\mathrm{v}}(|\boldsymbol{x}-\boldsymbol{R}_i|)\phi_{\mathrm{v}}^{k}(|\boldsymbol{x}-\boldsymbol{R}_k|)\Big\} \\ & + \int \mathrm{d}\boldsymbol{x}\Big\{\mu_{\mathrm{xc}}(n_{\mathrm{t}})\nabla_{R_k}n_{\mathrm{c}}^{k}(|\boldsymbol{x}-\boldsymbol{R}_k|) \\ & - n_{\mathrm{v}}(\boldsymbol{x})\frac{\mathrm{d}\mu_{\mathrm{xc}}(n_{\mathrm{t}})}{\mathrm{d}n_{\mathrm{t}}}\nabla_{R_k}n_{\mathrm{t}}^{k}(|\boldsymbol{x}-\boldsymbol{R}_k|)\Big\}.\end{aligned} \tag{A1.3}$$

The appearance of the core density in equations (A1.1) and (A1.3) arises from the non-linear dependence of the exchange–correlation energy and potential on the total density, n_{t}, which gives rise to a coupling between the valence and core densities that is calculationally inconvenient. Since core penetration by the valence orbitals is in general fairly weak and changes little as the nuclei move, the contribution of this coupling to the forces is usually unimportant and can be eliminated by invoking a description in which the core and valence densities appear separately. The valence-only functional

$$\begin{aligned}E_{\mathrm{v}}(\lambda_i,\alpha_i,\boldsymbol{R}_i) = {}& \sum_{n}^{\mathrm{v}}\tilde{a}_n C_i^n H_{ij} C_j^n - \int \mathrm{d}\boldsymbol{x}\; n_{\mathrm{v}}(\boldsymbol{x})\Big\{\tfrac{1}{2}\phi_{\mathrm{v}}(\boldsymbol{x}) \\ & + \mu_{\mathrm{xc}}[n_{\mathrm{v}}(\boldsymbol{x})] - \epsilon_{\mathrm{xc}}[n_{\mathrm{v}}(\boldsymbol{x})]\Big\} + \tfrac{1}{2}\sum_{i\neq j}\frac{Z_{\mathrm{v}}^{i}Z_{\mathrm{v}}^{j}}{|\boldsymbol{R}_i-\boldsymbol{R}_j|}\end{aligned} \tag{A1.4}$$

where the eigenvalues are calculated with exchange–correlation potential $V_{\mathrm{xc}}(\boldsymbol{x})\equiv\mu_{\mathrm{xc}}[n_{\mathrm{v}}(\boldsymbol{x})]+V_{\mathrm{xc}}^{\mathrm{c}}$, with $V_{\mathrm{xc}}^{\mathrm{c}}$ a stiff core potential, gives the energy of the valence electrons alone subject to the external potential $V_{\mathrm{ext}}\rightarrow V_{\mathrm{N}}+\phi_{\mathrm{c}}+V_{\mathrm{xc}}^{\mathrm{c}}$ of the nuclei and cores and the orthogonality constraints in equation (2). An appropriate choice for the exchange–correlation potential of the core is $V_{\mathrm{xc}}^{\mathrm{c}}(\boldsymbol{x})\equiv\mu_{\mathrm{xc}}[n^{\mathrm{at}}(\boldsymbol{x})]-\mu_{\mathrm{xc}}[n_{\mathrm{v}}^{\mathrm{at}}(\boldsymbol{x})]$,

where n^{at} and n_v^{at} are the total and valence densities of the neutral atom. The λ and α forces derived from equation (4) are again as given in equation (9), and the forces on the rigid cores are given by

$$\nabla_{R_k} E_v(\lambda_i, \alpha_i, R_i) = \sum_n^v \bar{a}_n C_i^n \left\{ \nabla_{R_k} [H_{ij} - \epsilon_n O_{ij}] \right\} C_j^n$$
$$+ \nabla_{R_k} \sum_{i \neq k} \left\{ \frac{Z_v^i Z_v^k}{|R_i - R_k|} - \int \mathrm{d}x \; n_{\lambda_i}^v(|x - R_i|) \phi_v^k(|x - R_k|) \right\}$$
$$- \int \mathrm{d}x \; n_v(x) \frac{\mathrm{d}\mu_{xc}(n_v)}{\mathrm{d}n_v} \nabla_{R_k} n_v^k(|x - R_k|). \tag{A1.5}$$

The above formulae assume vanishing overlap of core functions on adjacent sites but can be used also when the cores overlap weakly provided account is taken of the main consequence of core overlap, which is the Pauli repulsion due to interacting closed shells. The Pauli repulsion between any two cores can be estimated via additive core repulsion terms (Harris 1985). For two s cores $|c_i\rangle, |c_j\rangle$, for example, the direct core–core pair potentials are

$$\delta V_{ij}^c \approx -2\langle c_i | c_j \rangle \langle c_i | V_i + V_j | c_j \rangle \tag{A1.6}$$

where V_i and V_j are the atomic potentials. If the core orbitals are represented by Λ-functions the potential integrals can be evaluated analytically via

$$\langle c_i | V_i + V_j | c_j \rangle = (\epsilon_c^i + \epsilon_c^j) \langle c_i | c_j \rangle - 2\langle c_i | - \frac{\nabla^2}{2m} | c_j \rangle. \tag{A1.7}$$

Appendix 2. Analytic evaluation of overlap and kinetic matrix elements

The expansion theorems obeyed by the Λ-functions are given by Filter and Steinborn (1980) and further numerical properties and the evaluation of multi-centre integrals are discussed in detail by Trivedi and Steinborn (1982). Since some of the formulae in these papers are quoted incorrectly (for example, equation (4.10c) of Filter and Steinborn should read $\Delta n_3 = n_1 + n_2 - n_3 + 1$, while the kinetic energy integrals in Trivedi and Steinborn are incorrect), we reformulate some of the relevant expressions and quote explicitly the main formulae we have used to perform integrals needed for the evaluation of matrix elements. Using the expansion theorem, the overlap matrix for Λ-functions on different sites is

$$\Theta_{ij} = \langle \Lambda_{nL}(\alpha, r_i) | \Lambda_{n'L'}(\beta, r_j) \rangle$$
$$= \sum_{n''L''} S_{n'L'}^{n''L''}(\beta, R_{ji}) \langle \Lambda_{nL}(\alpha, r) | \Lambda_{n''L''}(\beta, r) \rangle$$
$$= \sum_{n''} S_{n'L'}^{n''L}(\beta, R_{ji}) \langle \Lambda_{nL}(\alpha, r) | \Lambda_{n''L}(\beta, r) \rangle. \tag{A2.1}$$

Matrix elements of the kinetic energy can be written

$$\begin{aligned} K_{ij} &= \langle \Lambda_{nL}(\alpha, \mathbf{r}_i) | -\frac{\Delta}{2} | \Lambda_{n'L'}(\beta, \mathbf{r}_j) \rangle \\ &= -\tfrac{1}{2} \langle \Delta \Lambda_{n,L}(\alpha, \mathbf{r}_i) | \Lambda_{n'L'}(\beta, \mathbf{r}_j) \rangle \\ &= -\frac{\alpha^2}{2} \sum_{n''L''} S_{n'L'}^{n''L''}(\beta, \boldsymbol{R}_{ji}) \langle \Delta \Lambda_{nL}(\alpha, \mathbf{r}) | \Lambda_{n''L''}(\beta, \mathbf{r}) \rangle \\ &= -\frac{\alpha^2}{2} \sum_{n''} S_{n'L'}^{n''L}(\beta, \boldsymbol{R}_{ji}) \langle \Delta \Lambda_{nL}(\alpha, \mathbf{r}) | \Lambda_{n''L}(\beta, \mathbf{r}) \rangle. \end{aligned} \tag{A2.2}$$

It can be shown that

$$\begin{aligned} \frac{\partial \Lambda_{nL}(\alpha, \mathbf{r})}{\partial r} &= -\alpha \Lambda_{n,L}(\alpha, \mathbf{r}) + \frac{n-1}{r} \Lambda_{n,L}(\alpha, \mathbf{r}) \\ &\quad - \frac{\sqrt{(n+l+1)(n-l-1)}}{r} \Lambda_{n-1,L}(\alpha, \mathbf{r}) \end{aligned} \tag{A2.3}$$

so that

$$\begin{aligned} \Delta \Lambda_{nL}(\alpha, \mathbf{r}) &= \left(\frac{\partial^2}{\partial r^2} + \frac{2}{r} \frac{\partial}{\partial r} - \frac{l(l+1)}{r^2} \right) \Lambda_{n,L}(\alpha, \mathbf{r}) \\ &= \alpha^2 \left\{ \left(1 - \frac{2n}{\alpha r} + \frac{n(n-1) - l(l+1)}{(\alpha r)^2} \right) \Lambda_{n,L}(\alpha, \mathbf{r}) \right. \\ &\quad + \frac{2(n+l+1)}{\alpha r} \sqrt{\frac{n-l-1}{n+l+1}} \left(1 - \frac{n-1}{\alpha r} \right) \Lambda_{n-1,L}(\alpha, \mathbf{r}) \\ &\quad \left. + \frac{\sqrt{(n+l+1)(n+l)(n-l-1)(n-l-2)}}{(\alpha r)^2} \Lambda_{n-2,L}(\alpha, \mathbf{r}) \right\} \end{aligned} \tag{A2.4}$$

The basic ingredients needed in calculating Θ_{ij} and K_{ij} are then the one-dimensional integrals

$$\begin{aligned} &\int_0^\infty \mathrm{e}^{(\alpha+\beta)r} r^{l'} L_{n-l-1}^{2l+2}(2\alpha r) L_{n'-l-1}^{2l+2}(2\beta r) \mathrm{d}r \\ &= \sum_{P'=0}^{n'-l-1} \sum_{P=0}^{n-l-1} \binom{n+l+1}{n-l-1-P} \binom{n'+l+1}{n'-l-1-P} \\ &\quad \times \frac{(-1)^{P+P'} (2\alpha)^P (2\beta)^{P'} (l'+P+P')!}{P! P'! (\alpha+\beta)^{l'+P+P'+1}} \end{aligned} \tag{A2.5}$$

for $2l \leqslant l' \leqslant 2l+2$.

Appendix 3. Three-centre integrals

Three-centre integrals occurring within our calculational scheme take the form,

$$\begin{aligned}
&\langle \Lambda_{nL}(\alpha, r_i)|F_{\lambda_k}(r_k)|\Lambda_{n'L'}(\beta, r_j)\rangle \\
&\qquad = (\alpha\beta)^{-3/2} \sum_{n_1L_1} \sum_{n_2L_2} \sum_{n_1'L_1'} \sum_{n_2'L_2'} C_{nL}^{n_1L_1n_2L_2} C_{n'L'}^{n_1'L_1'n_2'L_2'} \\
&\Lambda^*_{n_2L_2}(\alpha, \boldsymbol{R}_{ik})\Lambda_{n_2'L_2'}(\beta, \boldsymbol{R}_{jk})\langle \Lambda_{n_1L_1}(\alpha, r)|F_{\lambda_k}(r)|\Lambda_{n_1'L_1'}(\beta, r)\rangle \\
&\qquad = \sum_{n_2L_2} \sum_{n_2'L_2'} G^{nLn'L'}_{n_2L_2n_2'L_2'}(\alpha, \beta, \lambda)\Lambda^*_{n_2L_2}(\alpha, \boldsymbol{R}_{ik})\Lambda_{n_2'L_2'}(\beta, \boldsymbol{R}_{jk})
\end{aligned} \tag{A3.1}$$

where $F_{\lambda_k}(r_k)$ represents either the Coulomb potential or the exchange–correlation potential due to the site density at k, and where

$$\begin{aligned}
G^{nLn'L'}_{n_2L_2n_2'L_2'}(\alpha, \beta, \lambda) = (\alpha\beta)^{-3/2} \sum_{n_1L_1} \sum_{n_1'L_1'} \Big\{ & C_{nL}^{n_1L_1n_2L_2} C_{n'L'}^{n_1'L_1'n_2'L_2'} \\
& \times \langle \Lambda_{n_1L_1}(\alpha, r)|F_\lambda(r)|\Lambda_{n_1'L_1'}(\beta, r)\rangle \Big\}.
\end{aligned} \tag{A3.2}$$

The integrals $\langle \Lambda_{n_1L_1}(\alpha, r)|F_\lambda(r)|\Lambda_{n_1'L_1'}(\beta, r)\rangle$ are either analytic or can be determined to sufficient accuracy using an appropriate integration mesh with only a few points. However, very many integrals are needed and so the evaluation of three-centre integrals represents a time-limiting step in the calculation.

Appendix 4. Exchange–correlation matrix elements

We consider the evaluation of matrix elements $\langle i|\mu_{xc}|j\rangle$ in conjunction with a sum over site densities and a polynomial approximation to μ_{xc}, as in equation (19). Only non-diagonal elements with $i \neq j$, the hardest case, are considered. The term in equation (19) linear in the density then involves three-centre integrals of the form $\langle i|n_k|j\rangle$. These can be dealt with as for the Coulomb potential and so pose little additional computational cost. The quadratic and cubic terms involve four- and five-centre integrals whose evaluation is unnecessary because of the weakness of the overlap of the site densities. If S is a typical value for the orbital overlap integral then the density overlap integrals will typically be of order S^2. Consider the contributions to the matrix elements which devolve from the quadratic term in equation (19),

$$\langle i|\sum_{k,l} n_k n_l|j\rangle = \sum_k \langle i|n_k^2|j\rangle + \sum_{k\neq l} \langle i|n_k n_l|j\rangle. \tag{A4.1}$$

The first term on the right-hand side includes all on-site contributions of the form $\langle i|n_i^2|j\rangle$ that are of order S compared to $\langle i|n_i^2|i\rangle$. Retaining just this term is correct to leading order in S and results in the approximation for the exchange–correlation matrix elements

$$\langle i|\mu_{xc}|j\rangle_0 \equiv a_0 O_{ij} + \sum_k \langle i|a_1 n_k + a_2 n_k^2 + \cdots|j\rangle. \tag{A4.2}$$

This guarantees a stable simulation and results in, at worst, three-centre integrals of a form already dealt with.

The next level of approximation envisages the additional inclusion of all terms of next highest order in the overlap, i.e. nominally of order S^3,

$$\begin{aligned}\langle i|\mu_{xc}|j\rangle_1 \equiv\ & \langle i|\mu_{xc}|j\rangle_0 \\ & + \langle i|2a_2 n_i n_j + 3a_3(n_i^2 n_j + n_i n_j^2) + \cdots|j\rangle \\ & + \sum_{k\neq i,j} \langle i|2a_2(n_i n_k + n_j n_k) + 3a_3(n_i^2 n_k + n_k n_j^2) + \cdots|j\rangle. \end{aligned} \tag{A4.3}$$

The first set of additional terms is clearly the larger and can be calcuated by using the rotation properties of the spherical harmonics to eliminate one dimension in the integrals. The remaining two-dimensional quadratures can be performed efficiently using a sparce mesh in elliptic coordinates or by reading from pre-set interpolation tables. The weakness of the site-density overlap ensures that only near-neighbour sites need be included. The second set of terms involves three-site integrals and contributes significantly only when the sites approach closely. Since the interaction then will usually be strongly repulsive such configurations will be improbable in a thermal ensemble. In general, therefore, we expect these and other terms of higher order in the overlap to be negligible. If this is not the case (as for the high-density H systems treated in section 5, where bond lengths are small and close encounters relatively frequent), these elements can be calculated by translating $|j\rangle$ to site i or vice versa and using two-dimensional quadrature about the axis $i-k$ (or $j-k$). Alternatively, we can make an estimate of such terms that improves as they become larger. In practice, formulae of the form

$$\langle i|n_i n_k|j\rangle \approx \langle i|n_i^2|j\rangle N_{ki} \tag{A4.4}$$

where

$$N_{ki} = \langle n_{\lambda_k}(|\boldsymbol{x}-\boldsymbol{R}_k|)|n_{\lambda_i}(|\boldsymbol{x}-\boldsymbol{R}_i|)\rangle / \langle n_{\lambda_k}(|\boldsymbol{x}|)|n_{\lambda_i}(|\boldsymbol{x}|)\rangle \tag{A4.5}$$

is the overlap factor of the two site densities i and k, give quite reasonable estimates and allow the additional terms to be included as additive corrections to the $k=i$ terms already considered. Similarly, terms fourth order in the overlap can be estimated via

$$\langle i|n_k n_l|j\rangle \approx \langle i|n_k^2|j\rangle N_{lk}. \tag{A4.6}$$

Alternative ways of dealing with such contributions are available if the site densities are represented by analytical functions that obey a translation theorem. This is the case for low-Z elements, where a single Λ-function can be used, and may be possible in general.

Acknowledgments

We thank Detlef Hohl for bringing the work of Trivedi and Steinborn to our attention, for much valuable help and for his comments on the manuscript. A grant of CPU time by the HLRZ, Forschungszentrum Jülich, is gratefully acknowledged.

References

Barbee T W, Garcia A, Cohen M L and Martins J L 1989 *Phys. Rev. Lett.* **62** 1150
Baroni S and Gianozzi P 1992 unpublished
Becke A D 1991 *J. Chem. Phys.* **96** 2155
Brovman E G, Kagan Y and Kholas A 1972 *Sov. Phys.–JETP* **34** 1300; **35** 783
Car R and Parrinello M 1985 *Phys. Rev. Lett.* **55** 2471
Ceperley D M and Alder B J 1987 *Phys. Rev.* B **36** 2092
Filter E and Steinborn E O 1980 *J. Math. Phys.* **21** 2725
Finnis M W 1990 *J. Phys.: Condens. Matter* **2** 331
Foulkes W M C and Haydock R 1989 *Phys. Rev.* B **39** 12 520
Harris J 1985 *Phys. Rev.* B **31** 1770
Harris J and Hohl D 1990 *J. Phys.: Condens. Matter* **2** 5161
Hemley R J and Mao H K 1988 *Phys. Rev. Lett.* **61** 857
Hohl D, Natoli V, Ceperley D and Martin R 1992 *Bull. Am. Phys. Soc.* **37** 356
Jones R 1988 *J. Phys. C: Solid State Phys.* **21** 5735
Kohn W and Sham L J 1965 *Phys. Rev.* A **140** 1133
Lorenzana H E, Silvera I F and Goettel K A 1989 *Phys. Rev. Lett.* **63** 2080
Painter G S and Averill F W 1982 *Phys. Rev.* B **26** 1781
Pederson M R, Klein B M and Broughton J Q 1988 *Phys. Rev.* B **38** 3825
Perdew J P 1986 *Phys. Rev.* B **33** 8822
Polatoglou H M and Methfessel M 1988 *Phys. Rev.* B **37** 10 403
—— 1990 *Phys. Rev.* B **41** 5898
Read A J and Needs R J 1989 *J. Phys.: Condens. Matter* **1** 7565
Robertson I J and Farid B 1991 *Phys. Rev. Lett.* **66** 3265
Sankey O and Niklewski J 1989 *Phys. Rev.* B **40** 3979
Seifert G, Eschrig H and Bieger W 1986 *Z. Phys. Chem.* **267** 529
Trivedi H P and Steinborn E O 1982 *Phys. Rev.* A **25** 113
Vanderbilt D 1990 *Phys. Rev.* B **41** 7892
Zaremba E 1990 *J. Phys.: Condens. Matter* **2** 2479